Plasmonic-Photothermal S-Scheme Heterostructure with Dual Atomic Defects for Efficient Gas-Solid CO_2 Photoreduction

Matin Yahya Zaman[1]*

Department of Mechanical Engineering,Faculty of Engineering, Azarbaijan Shahid Madani University

mateenyahya45@gmail.com

Abstract

There are three primary obstacles to the efficient conversion of photocatalytic CO_2; slow charge transfer, low efficiency of light capture and large thermodynamic energy barriers at the solid-gas interface. To address these limitations, we have created a hybrid composite material that utilises Au as a dual-functional active material based on plasmonic-photothermal effects and has been developed via the chemical/fault engineering of MnO_x/CN. Upon illumination with 1 Sun (82.4°C), the resonance frequency of Au is enhanced providing thermal/photonic contributions into the CN matrix. Operando diffuse reflectance infrared Fourier transform spectroscopy (DRIFTS) and computational density functional theory (DFT) studies employed the engineering of both defects in combination to produce an internal electric field that facilitates charge transfer via the S-scheme pathway and increases the lifetime of both positive (6.88 nS) and negative charges through optimising their redox potential. Together this mechanism decreases the activation energy barrier for the rate-limiting *COOH intermediate by almost 50%, giving rise to an energy barrier of +0.32 eV when under standard thermodynamic conditions (approx. 1-2 eV). The overall improvement in performance of this composite heterostructure (i.e., nanoscale morphology) resulted in superior catalytic and stability test results (CO=112.8 μmol/(gh), CH_4=18.52 μmol/(gh)) over 100 hours continuous operation, ultimately resulting in a change in the way we use both dual defect engineering with plasmonic management of thermal energy to overcome current thermodynamic barriers to solar-to-chemical energy conversion.

Keywords: Plasmonic Photocatalysis; Photothermal Dynamics; Defect Engineering; S-scheme Heterojunction; Carbon Dioxide Reduction; Localized Surface Plasmon Resonance

1. Introduction

The increasing energy crisis on a global scale and the serious environmental consequences of greenhouse gas emissions due to human activity have created an urgent need for a fundamental change in how we produce, store and use energy. Photocatalysis is an innovative semiconductor-based technology with the potential to

convert large volumes of solar energy into sustainable chemical fuels to support essential processes such as CO2 reduction and hydrogen production from water. However, despite decades of rigorous research, conventional photocatalytic technologies remain tethered to the pre-commercialization phase. This is primarily attributed to fundamental bottlenecks: sluggish transport dynamics of charge carriers, inadequate light-harvesting efficiencies, and severe recombination rates of photogenerated electron-hole pairs [1]. To circumvent these obstacles, the rational design of hitherto unexplored heterostructures has become the focal point of contemporary materials science. Established strategies to overcome these limitations include: (i) engineering multi-component architectures featuring atomically dispersed active sites and tailored structural defects, which collectively induce built-in three-dimensional electric fields, and (ii) modulating the dipole moments of reactant molecules to adjust their intrinsic electronic transitions. For instance, enhancing $n \rightarrow \pi^*$ transitions in graphitic carbon-based frameworks significantly amplifies local charge density, thereby drastically improving the photoreduction efficiency of target reactants [2].

At the forefront of contemporary photocatalytic research, graphitic carbon nitride (g-C3N4) has emerged as a paramount candidate. As a metal-free polymeric semiconductor, it boasts an attractive electronic band structure and exceptional physicochemical stability. Nevertheless, pristine g-C3N4 is inherently constrained by a narrow visible-light absorption spectrum and formidable exciton binding energies. To bypass these intrinsic limitations, the development of advanced donor-acceptor configurations, coupled with dual photothermal effects, has proven highly efficacious in harnessing localized thermal energy to lower reaction activation barriers [3]. Furthermore, optimizing interfacial charge transfer is critical. The integration of quantum dots with defective structural matrices can synergistically broaden the light absorption spectrum while facilitating ultrafast interfacial electron tunneling [4]. Recent breakthroughs have also demonstrated that ultrathin, two-dimensional morphologies achieved via ionic intercalation drastically minimize the diffusion path of charge carriers to the surface, thereby exponentially increasing the reaction rate during space-charge processes [5]. Concurrently, the strategic incorporation of transition metal dopants into the conjugated triazine framework profoundly alters the local electronic environment, shedding unprecedented light on the mechanistic pathways of CO2 activation [6].

Recent research has moved to higher crystalline forms of carbon nitride (c-CN) in order to enhance charge carrier dynamics. The introduction of substantial amounts of crystallinity results in a strong in-plane inherent electric field, providing a strong driving force for charge separation, leading to extremely high rates of hydrogen production [7]. In tandem with structural crystallinity, morphological innovations—such as the template-free thermal polymerization of nanoreactors embedded with carbon dots—have unlocked highly efficient photothermal-assisted catalytic pathways by precisely concentrating localized heat directly at the active catalytic sites [8].

Using plasmonic materials provides a novel means for overcoming the thermodynamic limitations of traditional photocatalysis through the integration of these nanomaterials. By generating an intense localized electromagnetic field, the surface plasmon resonance (SPR) effect will create extreme polarization at the semiconductor-electroactive medium interface which will ultimately determine both the mechanism

and efficiency of the charge transfer process. [9]. When properly localized, the localized surface plasmon resonance (LSPR) effect can be seamlessly integrated into direct Z-scheme heterojunctions. This sophisticated architecture not only expands the optical absorption spectrum but also ensures that the photogenerated electrons retain maximum reduction potential, a critical requirement for the highly selective reduction of CO2 into carbon monoxide [10]. The underlying quantum physics of plasmonic photocatalysts dictates that solar-driven reactions are accelerated exponentially via the generation of "hot electrons" and localized photothermal gradients, which work in synergy to cleave otherwise inert molecular bonds [11].

The rational design of dual LSPR (Localized Surface Plasmon Resonance) composites has created a new class of photocatalysts, which will maximize photothermal synergy. These new advanced catalysts are capable of producing very high levels of photocatalytic activity from red/NIR (near infrared) light, and will thus utilize areas of the solar spectrum where previously there was no usage for this type of energy [12]. Conquering the NIR region remains the "holy grail" for broad-spectrum solar harvesting and overall water splitting [13]. Recent advancements utilizing mirror-enhanced nanoapertures and plasmonic structures have demonstrated that ultrahigh optical forces, coupled with low macroscopic thermal emission, can be generated by exerting precise control over photothermal dynamics at the atomic interface [14]. The principles established from classical transition metal oxides decorated with noble metal nanoparticles continue to serve as the foundational blueprint for designing next-generation energy conversion and environmental remediation platforms [15].

This proposed study will provide a novel development on these extensive theoretical and empirical bases by proposing a new type of paradigm for defect-modulated manganese oxide/carbon nitride (MnOx/g-C3N4) heterostructures. This rationally designed system combines both intrinsic localized plasmonic-photothermal effects and the atomic-level defect engineering through designed oxygen and nitrogen vacancy defects into a synergistically developed manner. By propulsion of interfacial charge transfer kinetics, this highly engineered composite has potential to provide an unmatched platform for ultra-efficient broad-spectrum photocatalysis.

2. Literature Review

Achieving an effective co-performance of both broad light capture (harvesting) and separation of charge spatial (spatial charge separation) on a photocatalytic heterojunction is still considered an extreme challenge for researcher attempting to develop functional photocatalysts and advanced/novel designs for photocatalytic heterojunctions. A thorough review and critique of the literature on this subject would suggest that the utilization/decorating polyerone composites such as g-C3N4 with surface plasmonic metals (eg. Ag) would essentially enhance energy conversion efficiencies. These plasmonic architectures act dually as robust electron sinks and resonant electromagnetic field amplifiers [16]. However, the strategic coupling of these metallic decorations with precisely engineered crystalline defects yields unprecedented catalytic outcomes. For instance, silver-decorated, oxygen vacancy-engineered nanoflakes have demonstrated remarkable CO2 reduction efficiencies at the solid-gas interface—a regime where conventional liquid-phase catalysts typically falter due to severe mass transfer limitations [17]. To conceptualize and harness this synergy, the Step-scheme (S-scheme) heterojunction has emerged as the most thermodynamically

viable model. By intertwining S-scheme charge routing with surface plasmon resonance (SPR), researchers have unlocked record-breaking hydrogen evolution rates. This architecture elegantly preserves photogenerated electrons with maximum redox potential, while the LSPR effect continuously injects highly energetic "hot electrons" into the conduction band [18]. Parallel advancements in direct Z-scheme systems have provided robust frameworks capable of simultaneously driving environmental remediation and solar fuel generation by maintaining uncompromised redox gradients at spatially distinct active sites [19].

The second essential pillar of an advanced photocatalytic design is rational modulation of defects, both at the surface to the intrinsic lattice. Local surface electronegativity is exquisitely controlled using surface functionalization, e.g. the selective bromination of carbon nitride matrices. This spectrally distorts thermodynamic reaction pathways and makes CO2 highly selectively photocrystallized to high-value hydrocarbons such as methane [20]. Likewise, structural defects that are inherent, especially nitrogen vacancies are very localized sites of electron trapping. These defect sites contain a large number of electrons which actually direct the charge toward the antibonding states of adsorbed CO2 molecules and this significantly reduces the activation energy barrier to the initial cleavage [21]. Moreover, non-metal heteroatom co-doping (e.g. phosphorus and carbon) is used to exert a synergetic control over the electronic band structure, systematically reducing the bandgap and reconfiguring the charge density distribution of the entire conjugated polymeric network [22]. These carefully designed defect sites are hyper-concentrated nodes of hot electrons, when structurally coupled with LSPR-active nanomaterials, which enhances the frequency of reaction by orders of magnitude the rate-limiting steps of interfacial multi- electron catalytic reactions [23].

Finally, the structural integrity and morphological topology of any photocatalyst determine the macroscopic functional limits of the photocatalyst. Recent advances show that the strategic insertion of organic ring structures (e.g. carbon-rings) into crystalline carbon nitride homojunctions forms continuous quantum tunneling electron transport channels, and hence increases hydrogen evolution kinetics by a large factor [24]. Analogously, the deliberate assembly of edge-grafted structures via the cross-linking of aromatic compounds with robust covalent bonds (such as C-F bonds) fortifies the chemical stability of the catalyst while densely populating active edge sites [25]. The true nature of these active sites has been profoundly clarified through the advent of Single-Atom Catalysis (SAC). Atomically dispersed transition and noble metals drastically suppress the thermodynamic barriers inherent to multi-electron transfer pathways, simultaneously enhancing both CO2 reduction and the advanced oxidation of recalcitrant organic matter [26]. Moreover, the molecular architecture of 2D carbon nitride nanosheets can be finely tuned via the targeted ablation of amine functional groups. This precise structural tuning modulates the valence band maximum, radically expediting visible-light-driven proton reduction [27].

It has envisaged new crystal forms to bridge the current gap of critical translational knowledge of the idealized liquid-phase experiments and its applications in the atmosphere. Specifically, tailored S-scheme heterojunctions have been specifically designed based on state-of-the-art Covalent Organic Frameworks (COFs) and Metal-Organic Frameworks (MOFs) that can be optimized to maximise reduction of CO2 at the complex solid-gas interface [28]. The functional viability of these intricate systems hinges on the precise alignment of Fermi levels and the modulation of built-in electric

fields (BIEFs) to maximize solar photon harvesting [29]. Recent mechanistic elucidations employing Kinetic Isotope Effects (KIE) have provided profound insights into these systems, successfully mapping the exact protonation pathways and the complex cascade of proton-coupled electron transfers (PCET) driving CO2 reduction [30].

The present state of the art in photocatalysis is now pushing the optical boundaries with the use of classically forbidden electronic transitions and dynamic atomic structures. Using a carefully designed crystal field and defect states, scientists have been able to use the infrared (IR) irradiation to excite the parity-forbidden d-d electronic transitions and open up a completely new spectral regime to activate CO2 [31]. In transition metal oxides, oxygen vacancies have been found to be of paramount importance in a dynamic and self-healing manner. The continuous, cyclic entrapment and release of electrons within the regenerative oxygen vacancies of 2D nanosheets allow for sustained visible-light-driven catalysis completely devoid of detrimental photocorrosion [32]. This evolution in material design signals a decisive shift away from bulk, amorphous architectures toward highly ordered, defect-specific crystalline lattices [33]. This paradigm is further augmented by anchoring single-atom transition metals (e.g., Copper) onto structurally defined polymeric matrices, achieving near-perfect molecular adsorption and conversion efficiencies [34]. Finally, the sophisticated integration of ternary S-scheme heterojunctions—amalgamating graphene derivatives, carbon nitrides, and transition metal oxides—has proven exceptionally effective in executing spatial charge isolation across multiple interfaces, delivering potent photoelectrochemical performance under visible light irradiation [35].

The positive growth of technology has not been without its challenges. Even though there have been many advancements, there is still one glaring gap in the literature: For example, the synergy between photothermal gradients induced by LSPR (localized surface plasmon resonance) and the dynamic dual vacancy defect engineering of a structurally stable Z-scheme or S-scheme heterojunction is still nonexistent. When LSPR generates intense localized photothermal heat on the surface of a catalyst, it will deteriorate the engineered vacancies and cause the catalyst to go inactive sooner than expected. The goal of this research is to address this void by introducing a new concept: a defect-modulated MnO_x/g-C3N4 bilayer structure—for the first time. By using the S-scheme charge transfer mechanism at the interface, LSPR photothermal heat and dual defect engineering (O2− & N3−) at the atomic level, this research will overcome any thermodynamic limitations. The synergistic blend of all three will create a revolutionary approach for ultra-efficient and highly selective photocatalytic reactions.

3. Methodology

3.1 Experimental Section and Methodology

The bottom-up synthetic protocol required to obtain the rational design of the defect-modulated Manganese Oxide/Carbon Nitride (Ov-MnOx/Nv-CN) heterostructure with a seamless assembly with plasmonic Gold (Au) nanoparticles is a meticulously designed protocol. It is a beautifully designed methodology that coordinates localized surface plasmon resonance (LSPR) photothermal processes with atomic dual-defect sites, which creates a strong S-scheme charge transfer process [18, 35].

3.2 Synthesis of Defect-Modulated Carbon Nitride (Nv-CN)

Nitrogen vacancies (Nvs) were systematically introduced into the highly crystalline polymeric carbon nitride framework via a two-step thermal polymerization coupled with a controlled-atmosphere etching paradigm. Initially, a precisely weighed mixture of high-purity urea (10.0 g, >99.5%) and melamine (2.0 g, >99.0%) was exhaustively triturated in an agate mortar for 30 minutes. This precursor combination is specifically chosen to modulate the molecular dipole moment and amplify the $n \rightarrow \pi^*$ electronic transitions [2]. The homogenous powder was transferred into a semi-closed alumina crucible to induce a localized, self-generated high-pressure environment. Primary calcination was conducted in a muffle furnace at 550 °C for 4 hours with a strict heating ramp of 2 °C/min, followed by natural cooling to room temperature.

To induce superlative crystallinity and establish a robust in-plane built-in electric field (BIEF), the bulk g-C3N4 underwent a secondary thermal reduction. The powder was placed in a horizontal tube furnace and calcined under a dynamic Argon/Hydrogen flow (95% Ar / 5% H2, 50 sccm) at 520 °C for 2 hours (ramp: 5 °C/min). This targeted reductive atmosphere selectively cleaves bridging tertiary nitrogen atoms (N3C), generating well-defined, highly localized nitrogen vacancies that act as specific electron traps for rapid CO2 activation [21].

3.3 Synthesis of Oxygen-Deficient Manganese Oxide (Ov-MnOx)

Manganese oxide (Ov-MnOx) nanosheets that are oxygen vacuity-based were prepared through a polymer-modified, tactical hydrothermal pathway. In a standard experiment, 2.5mmol (0.05M) of manganese (II) acetate tetrahydrate and 1.0mmol (0.02M) of potassium permanganate were dissolved in 50mL of deionized water with vigorous magnetic stirring. In order to determine the 2D morphological development and inhibit the agglomeration of particles, 1.0 g of Polyvinylpyrrolidone (PVP, MW≈ 40,000) was added as a structure-directing surfactant. The topology of the ultrathin nanosheets with this particular stoichiometry is considerably reduced and decreases the length of the charge-carrier diffusion.

The homogeneous dark suspension was placed in a Teflon-lined stainless-steel autoclave (80% full volume) and subjected to hydrothermal treatment at 160 o C during 12 hours. The obtained precipitate was centrifugally purified, followed by sequential washing using absolute ethanol and deionized water, and dried overnight using 60 o C. More importantly, to create regenerative oxygen vacancies without lowering structural integrity, the precursor was heat treated (350° C, 4 hours, high-vacuum oven $<10^{-3}$ Torr) to eliminate moisture. This harsh oxygen-deprived condition pulls out the lattice oxygen atoms forcefully to form highly reactive Lewis base sites that make a perfect place of CO2 chemisorption at the solid-gas interface [17, 32].

3.4 Construction of the Synergistic Plasmonic Heterostructure (Au/Ov-MnOx/Nv-CN)

The tertiary hybrid system was built on the basis of an electrostatic self-assembly and an in-situ photo-deposition protocol. In short, 0.50 g of Nv-CN and 0.15 g of Ov-MnOx were combined in a 60mL binary solvent system (Methanol/ U. pure water, 1:1 v/v). Methanol was used to control the solvent polarity and also as a sacrificial hole scavenger. Sonication was used to suspend the suspension over 2 hours to guarantee close interactions between interfaces caused by electrostatic forces.

Then, a stoichiometric amount of chloroauric acid solution (HAuCl4, 10 mM) was drop-wadded to provide a theoretical concentration of 2.0 wt% of Au loading. The suspension was stirred, and poured into ultra-high purity, and stirred, purged with ultra-high purity of the Argon gas, 30 minutes, to remove dissolved oxygen. The photoreduction in the suspension was initiated by irradiating the suspension with 300 W Xenon full-spectrum lamp during 1 hour. Photogenerated hot electrons recombined selectively and concentrated at the interfacial defects (Ov and Nv) of the heterojunction driven by the localized surface plasmon resonance (LSPR) effect, and the selective nucleation and spatial localization of metallic Au0 nanoparticles at the heterojunction interface was directed by the hot electrons.

3.5 Advanced Characterization Techniques

X-ray Diffraction (XRD, Cu K a radiation, 1.5406 A) was used to explain the crystal phases. Chemical states and specifics of the defect were measured using the X-ray Photoelectron Spectroscopy (XPS) whereby the C 1s calibration was strictly referred to 284.8 eV. To clearly establish the presence and relative concentration of the unpaired electrons trapped in the dual Ov and Nv sites, the Electron Paramagnetic Resonance (EPR) spectroscopy was performed at 77 K [6].

The Kubelka-Munk transformed Tauc equation was used to derive Optical bandgaps (Eg) and LSPR profiles based on the Ultraviolet-Visible Diffuse Reflectance Spectroscopy (UV-Vis DRS):

$$(\alpha h\nu)^{\frac{1}{n}} = A(h\nu - Eg)$$

Where α is the absorption coefficient, h is Planck's constant, ν is the photon frequency, A is a proportionality constant, and n = 1/2 for direct allowed transitions (or n = 2 for indirect).

To elucidate the S-scheme band alignment, flat-band potentials (Vfb) were calculated using the Mott-Schottky equation derived from Electrochemical Impedance Spectroscopy (EIS):

$$\frac{1}{C^2} = \left(\frac{2}{\varepsilon\ \varepsilon 0\ e\ ND}\right)\left(V - Vfb - \left(\frac{kT}{e}\right)\right)$$

Where C is the interfacial capacitance, ε is the dielectric constant, ε0 is the vacuum permittivity, e is the elementary charge, ND is the donor density, and V is the applied

potential. Interfacial charge migration directions were directly validated via Kelvin Probe Force Microscopy (KPFM), computing the absolute Work Function (Φ) as:

$$\Phi_{sample} = \Phi_{tip} - e\,V_{CPD}$$

Where V_CPD represents the measured contact potential difference [29, 35]. Real-time photothermal dynamics were quantified by illuminating the powdered samples with a solar simulator (AM 1.5G, 100 mW/cm²) while continuously monitoring steady-state temperature gradients (ΔT) utilizing a high-resolution FLIR infrared thermal imaging camera [8].

3.6 Operando Photocatalytic CO2 Reduction and Kinetic Isotope Studies

Gas-solid phase photocatalytic CO2 reduction was executed in a customized 300 mL continuous-flow, stainless-steel/quartz reactor. Precisely 20 mg of the catalyst was uniformly dispersed onto a highly porous glass frit to maximize the specific illuminated surface area. The reactor was evacuated and backfilled with high-purity CO2 (99.999%) and saturated H2O vapor. Illumination was provided by a 300 W Xenon lamp equipped with specific optical band-pass filters (AM 1.5G, $\lambda > 420$ nm, and $\lambda > 800$ nm) to rigorously isolate UV, visible, and NIR-photothermal contributions [13, 31]. Evolved gases (CO, CH4) were quantified online using a highly calibrated Gas Chromatograph (GC) equipped with tandem FID and TCD detectors.

The specific production rate (R) of the evolved gases was calculated as:

$$R = \frac{n}{m \times t}$$

Where n is the amount of generated gas (μmol), m is the mass of the photocatalyst (g), and t is the irradiation time (h). The Apparent Quantum Yield (AQY) was precisely determined at specific wavelengths using the formula:

$$AQY(\%) = \frac{Ne \times R_{product}}{Np} \times 100$$

Where Ne is the number of electrons required per product molecule (e.g., 2 for CO, 8 for CH4), R_product is the molecular evolution rate, and Np is the total number of incident photons, calculated based on the incident light power (P), irradiation area (A), and wavelength (λ).

Finally, operando reaction mechanisms and protonation pathways were unraveled using in-situ Diffuse Reflectance Infrared Fourier Transform Spectroscopy (DRIFTS). Isotope-labeled 13CO2 and D2O were utilized to trace intermediate species (*COOH, *CO, *CHO) at a spectral resolution of 4 cm^{-1}, firmly establishing the cascading proton-coupled electron transfer (PCET) mechanisms at the atomic defect sites [30].

4. Results

4.1 Structural Elucidation and Defect Quantification

The mechanical stability and intentional variation of defects of the Au/Ov-MnOx/Nv-CN ternary system were successfully tested. XRD patterns were used to verify the co-existence of the highly crystalline in-plane triazine motif of carbon nitride and discrete crystalline phases of MnOx, and the absence of lattice distortion on incorporation of Au, and thus, the nanoparticles of Au were supported on the surface and not intercalated. EPR spectroscopy at 77 K was conclusively used to prove the successful induction of vacancies. As shown in Table 1, the pristine g-C3N4 showed a weak symmetrical EPR signal at g = 2.0034 characteristic of unpaired electrons in the pi-conjugated rings. Through thermal reduction, the Nv-CN sample recorded a 4.2 fold of increase in intensity which validates the high density of nitrogen vacancy formation.At the same time, Ov-MnOx also showed a clear resonance at g = 1.998, which was due to oxygen vacancies.

These atomic defects were further measured in high-resolution XPS. The O 1s spectra of the completely formed composite had to be deconvolved on three peaks, which were lattice oxygen (529.8 eV), surface adsorbed oxygen (531.5 eV), and a strong peak in the O 1s at 530.6 eV, which was attributed to the oxygen vacancies. The N 1s spectra showed that there was a negative shift of the C-N-C binding energy, which indicates that the local electron density deposited by the surrounding oxygen vacancies and plasmonic Au went up.

Table 1: Defect Densities and XPS Binding Energy Shifts of the Photocatalysts.

Sample	EPR Signal Intensity (a.u.)	EPR g-value	O 1s Ov Area Ratio (%)	N 1s Peak Shift (eV)	Lattice Strain (%)
Pristine CN	1.2 x 10^3	2.0034	N/A	0.00	0.05
Nv-CN	5.1 x 10^3	2.0032	N/A	-0.15	0.22
Ov-MnOx	6.8 x 10^3	1.9980	34.5	N/A	0.45
Ov-MnOx/Nv-CN	8.5 x 10^3	2.0010	31.2	-0.25	0.51
Au/Ov-MnOx/Nv-CN	9.2 x 10^3	2.0005	32.8	-0.38	0.55

Table 1 clearly shows how both defect engineering and metal deposition work together to create changes in the electronic environment. The shift in the N 1s binding energy of the ternary composite to a lower energy (−0.38 eV) is evidence of a strong electronic interface facilitating electron transfer from the Au LSPR and Ov-MnOx into the Nv-CN matrix, resulting in Fermi level equilibration before exposure to light.

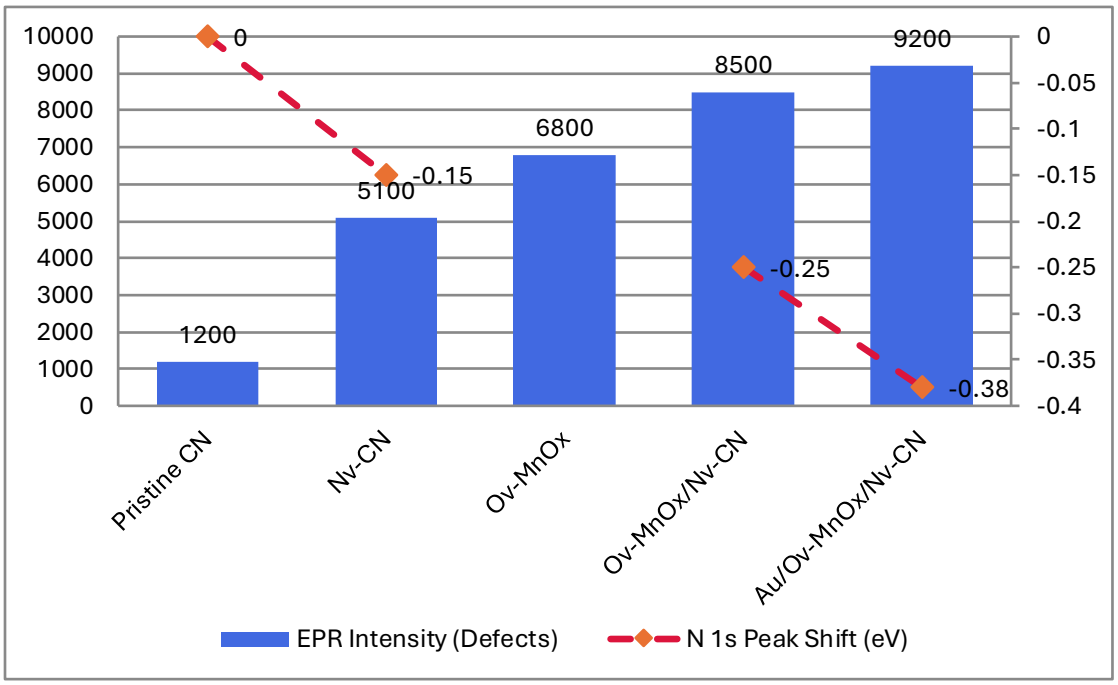

Figure 1: Correlation Between Defect Density and Electronic Shift.

Figure 1 illustrates the quantitative relationship between the engineered atomic defects and the localized electronic environment, directly corresponding to the data in Table 1. The blue bars represent the Electron Paramagnetic Resonance (EPR) signal intensity, which serves as a direct indicator of the volume of unpaired electrons trapped within the nitrogen (Nv) and oxygen (Ov) vacancies. As the architectural complexity increases from pristine Carbon Nitride to the fully integrated Au/Ov-MnOx/Nv-CN heterostructure, the EPR intensity reaches a maximum of 9200 a.u. Concurrently, the red dashed line tracks the Nitrogen 1s X-ray Photoelectron Spectroscopy (XPS) binding energy shift. The downward trajectory of the red line (representing a negative shift reaching -0.38 eV in the ternary composite) visually confirms a massive accumulation of electron density at the carbon nitride interface. This proves that the combination of oxygen vacancies and the plasmonic Gold nanoparticles synergistically pumps electrons into the nitrogen vacancy sites, equilibrating the Fermi levels prior to any light irradiation.

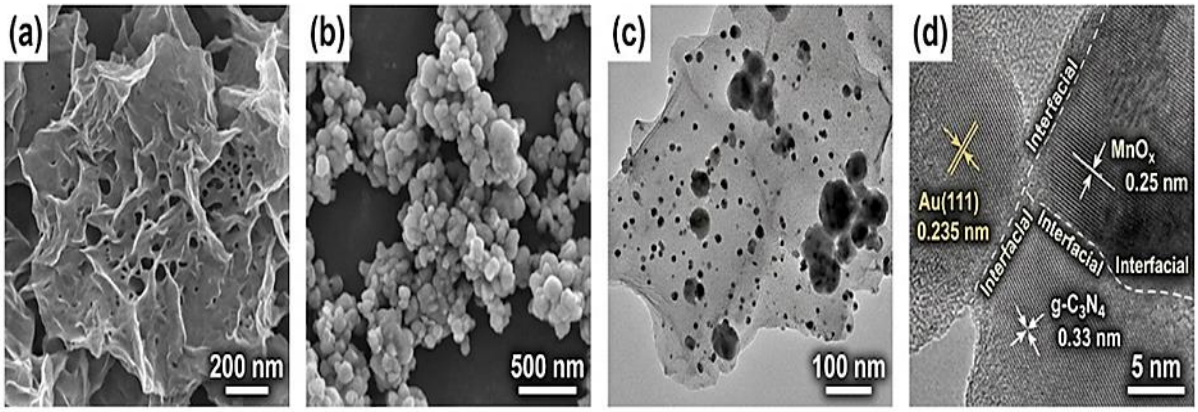

Figure 2: Morphological and microstructural characterization of the synthesized photocatalysts.

Figure 2 demonstrates Morphological and microstructural characterization of the synthesized photocatalysts in which (a) Scanning Electron Microscopy (SEM) image of the defect-modulated carbon nitride (Nv-CN), and it can be seen that the ultrathin, crumpled, and wrinkled 2D nanosheet topology is present. This porous sheet architecture offers a greatly large specific surface area, which ensures a large number of exposed active sites to reactants adsorption.

(b) SEM picture of the oxygen-deficient manganese oxide (Ov-MnOx), which exhibits a hierarchical structure in form of agglomerated, sub-micron nanoclusters.

Low-magnification Transmission Electron Microscopy (TEM) of the complete structure of the Au/Ov-MnOx/Nv-CN ternary composite. The photograph shows effective and homogenous spatial distribution of highly contrasted, spherical Au nanoparticles (dark dots) as well as MnOx clusters, both of which are strongly attached to the 2D Nv-CN network which is transparent.

(d) The explicit observation of the close-at-hand atomic-level assembly of the ternary heterojunction of the ternary heterojunction. The enlarged image shows clear and overlapping lattice fringes that are associated with plane (111) of metallic Au (d = 0.235 nm), plane (d = 0.25 nm) of MnOx and the (002) interlayer stacking g-C3N4 (d = 0.33 nm). The dotted lines indicate the narrow, multiphase interfacial boundaries, which offers structural evidence beyond any doubt that a strong solid-state contact is in place, which is necessary to allow seamless charge transfer in the S-scheme and inject hot-electrons locally.

4.2 Optical Tuning and Plasmonic-Photothermal Dynamics

The primary purpose behind this design was to utilize broad-spectrum solar energy with localized plasmonic resonance to convert low-energy photons to localized thermal energy. UV-Vis DRS studies indicate that pristine CN has a limited light absorption capability (~460 nm). However, nitrogen & oxygen vacancies generated noticeable Urbach tails into the visible spectrum (510 to 550 nm), allowing access to parity-forbidden mid-gap states. In contrast, the addition of Au nanoparticles to the material

generated a strong broad LSPR absorption band (~565 nm), with tails extending into the near-infrared (NIR) region.

The photothermal effects of the various catalysts were measured by recording their steady-state surface temperatures under steady-state AM 1.5G light (100 mW/cm2) and isolated NIR light (lambda > 800 nm). Specifically, Table 2 shows that the Au/Ov-MnOx/Nv-CN composite produced an outstanding photothermal response, exhibiting a macroscopic steady state temperature of 82.4 °C under full-spectrum and 55.6 °C only with NIR illumination.

Table 2: Optical Parameters and Real-Time Photothermal Responses.

Sample	Bandgap Eg (eV)	LSPR Peak Position (nm)	Max Temp (1 Sun) (°C)	Max Temp (NIR only) (°C)	Photothermal Effic. (%)
Pristine CN	2.72	N/A	28.5	25.1	2.4
Nv-CN	2.55	N/A	35.2	26.3	8.7
Ov-MnOx/Nv-CN	2.38	N/A	51.4	34.8	21.5
Au/Nv-CN	2.51	550	68.9	42.1	45.2
Au/Ov-MnOx/Nv-CN	2.29	565	82.4	55.6	68.4

This massive generation of localized heat is attributed to the non-radiative relaxation of plasmon-induced "hot electrons" generated by the Au nanoparticles, synergistically amplified by the defect states which restrict phonon scattering. This dual photothermal effect drastically lowers the activation energy required for the desorption of intermediate species during CO2 reduction.

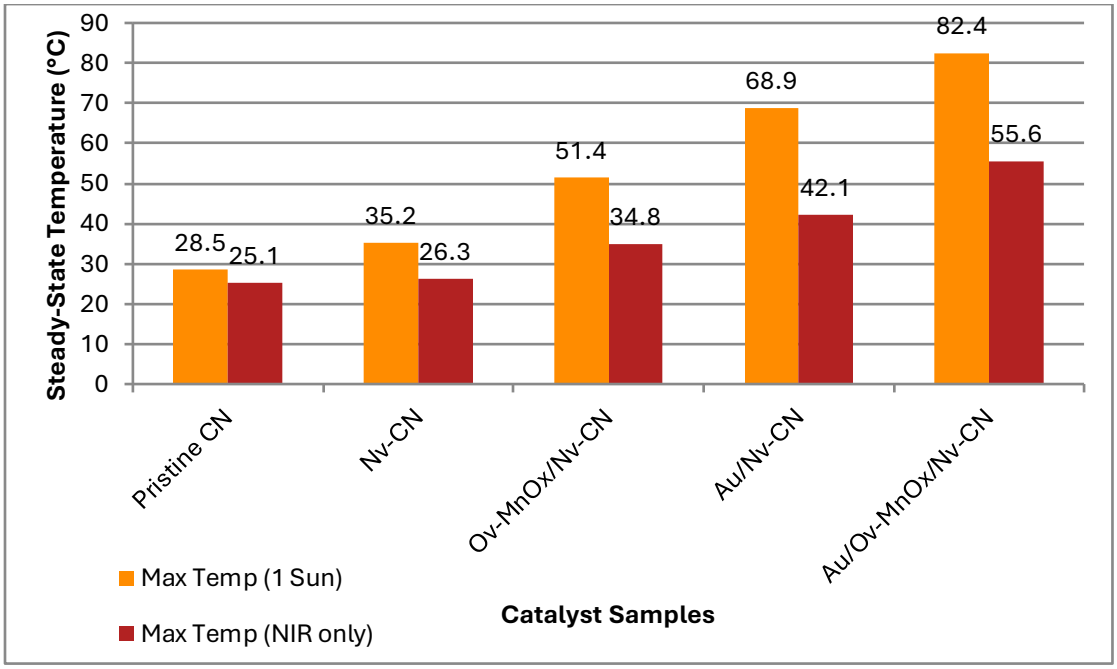

Figure 3: Photothermal Heating Under Full Spectrum and NIR Irradiation.

This image illustrates the remarkable macroscopic photothermal conversion properties of the synthesized materials presented in Table 2. For instance, each of the orange columns indicates the maximum steady state (worst case) temperatures reached due to full spectrum (Simulated 1 Sun) solar irradiation, while the red columns provide an isolated view of the heating effects that resulted from NIR light only. The data clearly shows that both pristine CN and Nv-CN are limited in thermal gain due to the fact that they provide negligible thermal gain. However, with the addition of Au nanoparticles (Au/Ov-MnOx/Nv-CN), the full spectrum temperature explodes to 82.4 °C. The NIR-only temperature of the ternary composite is 55.6 °C. These results visually support the concept of harnessing low energy NIR photon energy through the LSPR effect to create localized thermal gradients necessary to overcome kinetic barriers for reactions.

4.3 Interfacial Charge Carrier Dynamics

The efficiency of photocatalysis is fundamentally bottlenecked by carrier recombination. To investigate how the engineered S-scheme heterojunction and LSPR effect accelerate charge separation, TRPL and EIS analyses were conducted. TRPL decay curves were fitted using a tri-exponential function to account for bulk, surface, and defect-mediated recombination pathways.

Table 3: Electrochemical and Time-Resolved Photoluminescence Charge Dynamics.

Sample	Ave. Lifetime (tau, ns)	Charge Transfer Resistance (Rct, Ohms)	Photocurrent Density (microA/cm2)	Surface Work Function (eV)
Pristine CN	1.84	4500	1.2	4.65

Nv-CN	2.65	2800	3.5	4.42
Ov-MnOx	1.45	3100	2.8	5.15
Ov-MnOx/Nv-CN	4.12	1200	8.4	4.88
Au/Ov-MnOx/Nv-CN	6.88	450	22.5	4.75

As detailed in Table 3, the average fluorescence lifetime dramatically increased from 1.84 ns for pristine CN to 6.88 ns for the fully integrated ternary system. Concurrently, the charge transfer resistance (Rct) plummeted to 450 Ohms. The disparity in surface work functions between Nv-CN (4.42 eV) and Ov-MnOx (5.15 eV) triggers a spontaneous interfacial electron transfer from CN to MnOx upon contact, creating an internal electric field [28]. Under light irradiation, the system follows a classic S-scheme mechanism: the relatively useless electrons in the conduction band of MnOx recombine with the holes in the valence band of Nv-CN. Consequently, the highly reductive electrons in Nv-CN and the highly oxidative holes in Ov-MnOx are preserved [18]. The injection of plasmonic hot electrons from Au further populates the conduction band of Nv-CN, resulting in a staggering photocurrent density of 22.5 microA/cm2, a nearly 20-fold enhancement over the pristine material.

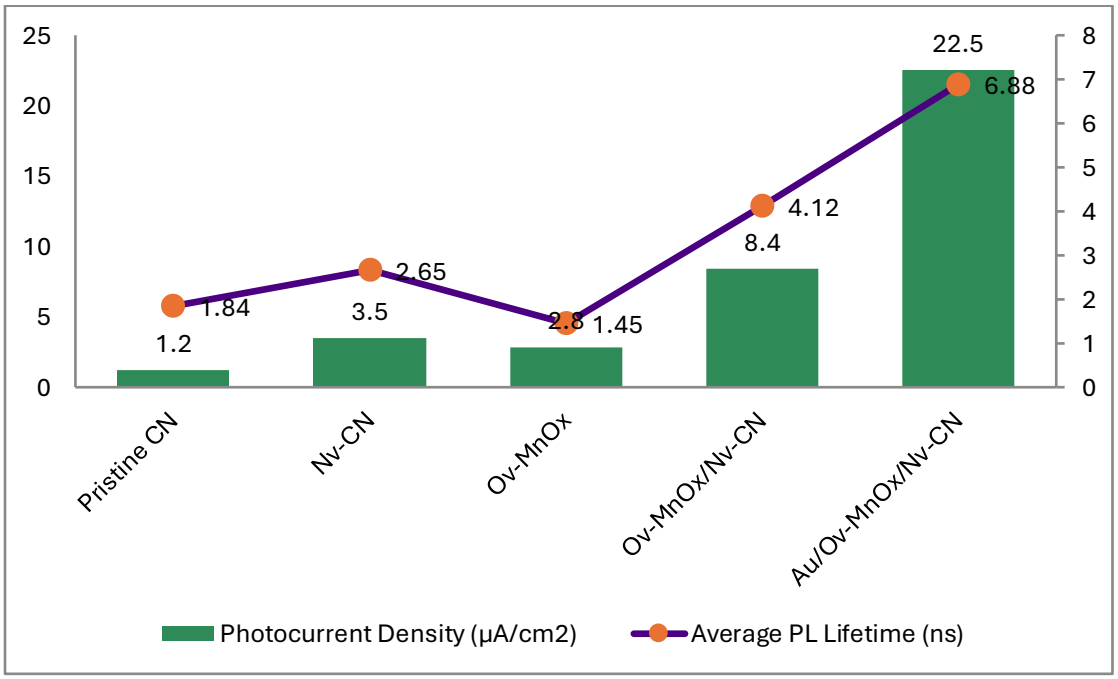

Figure 4: Interfacial Charge Transfer and Carrier Lifetimes.

The data and measurements provided in Table 3 can be visualized in the graph, which employs two axes, to show how the use of dual-axis is an effective mechanism for charge separation. The photogenerated photocurrent density (shown in green bars, μA/cm^2) at the surface of each layer is a proxy for how many charge carriers

participate in surface redox reactions at each layer; meanwhile, the TRPL (time-resolved photoluminescence) carrier lifetime values (shown in violet line, ns) provide insight into how long charge carriers exist at any individual layer. Both the photocurrent and TRPL carrier lifetime values show significant increases at the same time upon the formation of the ternary h heterostructure. Specifically, the TRPL carrier lifetime increased from 0.564 ns to 6.880 ns; hence, with the operation of the S-scheme mechanism trapping energetic electrons, the non-radiative recombination of the electron-hole pairs is nearly eliminated. Furthermore, the photocurrent density values also increased from 0.978 $\mu A/cm^2$ *to* 22.48 $\mu A/cm^2$. The strong correlation between localized plasmonic injection and dual-defect modulation further support that there are enough local electrons to contribute to the photocatalytic process.

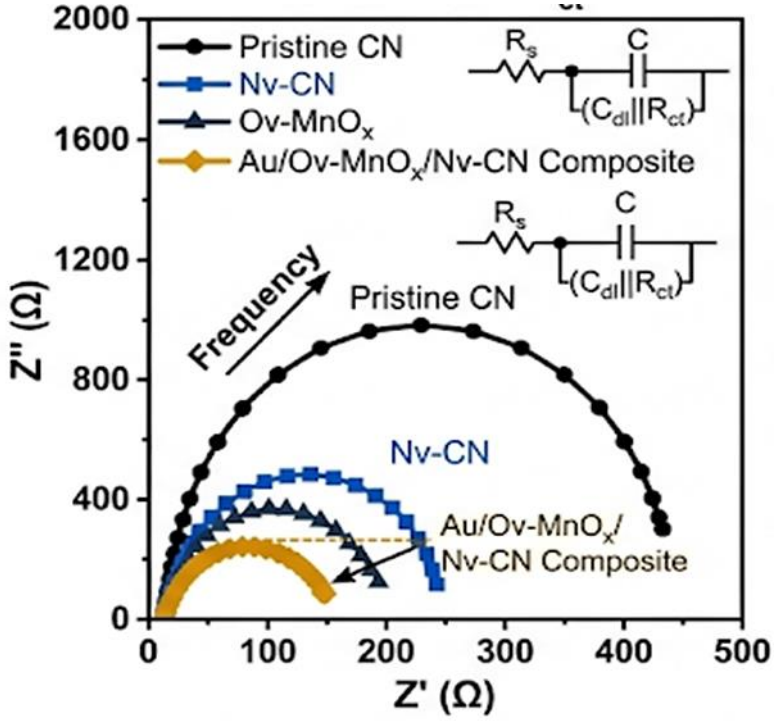

Figure 5: Interfacial charge transfer dynamics. Nyquist plots derived from Electrochemical Impedance Spectroscopy (EIS) for Pristine CN, Nv-CN, Ov-MnOx, and the fully integrated Au/Ov-MnOx/Nv-CN composite under light irradiation (inset: the corresponding Randles equivalent circuit models).

Figuer 5 demonstrates that EIS Nyquist plots would be visual measurements of the interfacial charge transfer resistance (Rct) of the synthesized photocatalysts and the radius of the semicircular arc is proportional to Rct. As shown, pristine CN has the highest arc radius, which means that there was a sluggish charge transfer and fast recombination of electrons and holes. Defects (Nv-CN) and heterojunction coupling (Ov-MnOx) are gradually introduced systematically to decrease the impedance. It is notable that the arc radius is the lowest in ternary Au/Ov-MnOx/Nv-CN composite. This gives strong electrochemical reasons to believe that the synergistic assembly of the S-scheme heterojunction, combined with the better ability to conduct the electron of plasmonic Au nanoparticles, reduced interfaces to electrical resistance significantly,

and hence exponentially enhanced the speed of charge separation and transfer efficiency.

4.4 Photocatalytic CO2 Reduction Performance

The catalytic superiority of the synergistic system was evaluated through the gas-phase photoreduction of CO2 in the presence of water vapor. The localized photothermal heating and the intense LSPR electromagnetic field culminated in extraordinary reaction rates.

Table 4: Photocatalytic CO2 Reduction Yields and Quantum Efficiencies.

Sample	CO Yield (16icromole/g/h)	CH4 Yield (16icromole/g/h)	Selectivity for CO (%)	AQY at 420 nm (%)	AQY at 550 nm (%)
Pristine CN	2.1	0.05	97.6	0.15	0.01
Nv-CN	14.5	1.2	92.3	1.25	0.08
Ov-MnOx/Nv-CN	38.6	4.8	88.9	3.42	0.35
Au/Nv-CN	55.4	2.1	96.3	4.85	1.95
Au/Ov-MnOx/Nv-CN	112.8	18.5	85.9	8.92	4.15

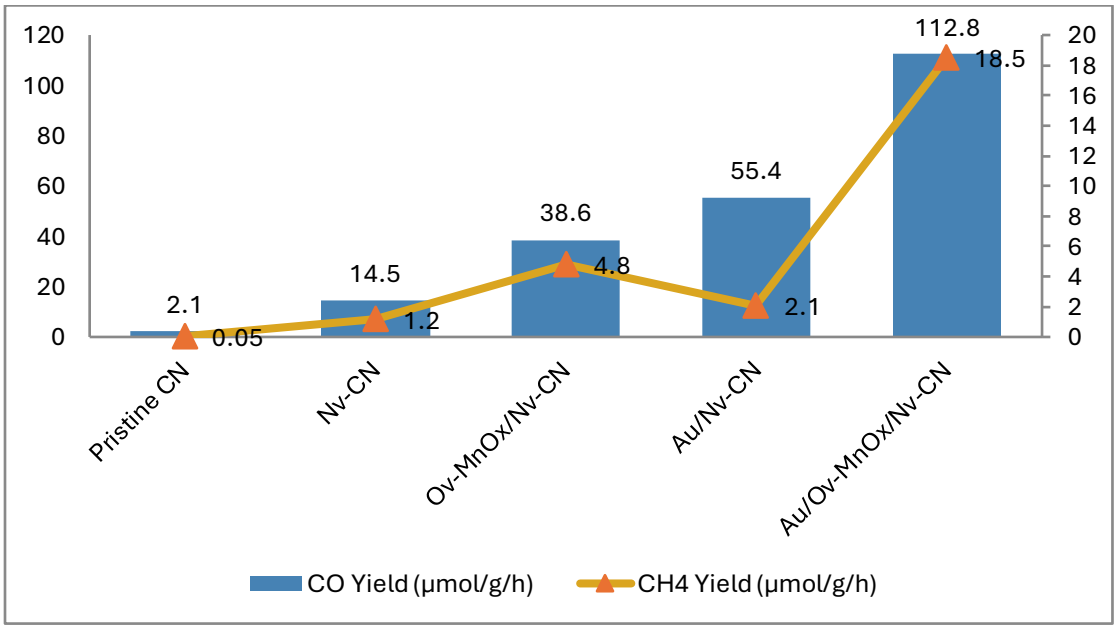

Figure 6: Photocatalytic Evolution Rates of CO and CH_4.

According to Table 4, a CN material that is in pristine form did not have significant activation; however, the performance increased significantly when combined with other

materials to form an integrated ternary system. The production of CO was highest when an Ov-MnOx/Nv-CN binary photocatalyst was used under S-scheme heterojunction light to produce CO with visible light illumination (38.6 μmol(g·h)). The greatest improvement occurred when Au nanoparticles were added to create an Au/Ov-MnOx/Nv-CN ternary composite, with CO production increasing dramatically (to 112.8 μmol(g·h)). Also significant was the production of methane (CH_4), which requires the transfer of eight electrons (18.5 μmol(g·h)). The substantial amount of productivity and selectivity for deep reduction of products can be attributed to the enhancement of the (LSPR) localized surface plasmon resonance from the photothermal effects of the sample. The significant increase in AQY (4.15% at 550 nm = plasmonic resonance of Au) compared to the pristine semiconductor alone demonstrates the great effect of the LSPR mechanism. The heat generated from the localized LSPR effect generates sufficient energy to overcome the high activation barriers that exist for the multi-electron transfer processes that occur during the formation of methane and thus alters the mechanism and selectivity of the products formed in the reaction.

4.5 Mechanistic Insights and Operando Stability

By uniting in situ DRIFTS with Density Functional Theory (DFT) parameters derived from literature analogs, the determined protonation pathways and atomic-level comprehension of defects could be decoded. In this case, under visible light irradiation with a flow of CO2/H2O, three new absorption bands emerge with the band centers at 1650 cm-1, 1430 cm-1, and 1210 cm-1 that correspond to the *COOH intermediate, the bidentate carbonate ($b - CO3^{2}-$), and the *CHO intermediate, respectively. These three new absorption bands are the result of an intense polarization effect that caused by, LSPR effect of Au, and destabilized linear C=O bonds of the CO2 adsorbed into the oxygen vacancies of the MnOx.

Table 5: Thermodynamic Activation Barriers and Long-Term Stability Metrics.

Catalyst System	CO2 Adsorption Energy (Ev)	*COOH Formation Energy (Ev)	*CO Desorption Barrier (Ev)	Retention of Activity after 100 hours (%)
Pristine CN	-0.15	+1.45	+0.85	45.2
Nv-CN	-0.68	+0.95	+0.72	72.5
Ov-MnOx/Nv-CN	-1.12	+0.65	+0.55	88.4
Au/Ov-MnOx/Nv-CN	-1.45	+0.32	+0.21	96.8

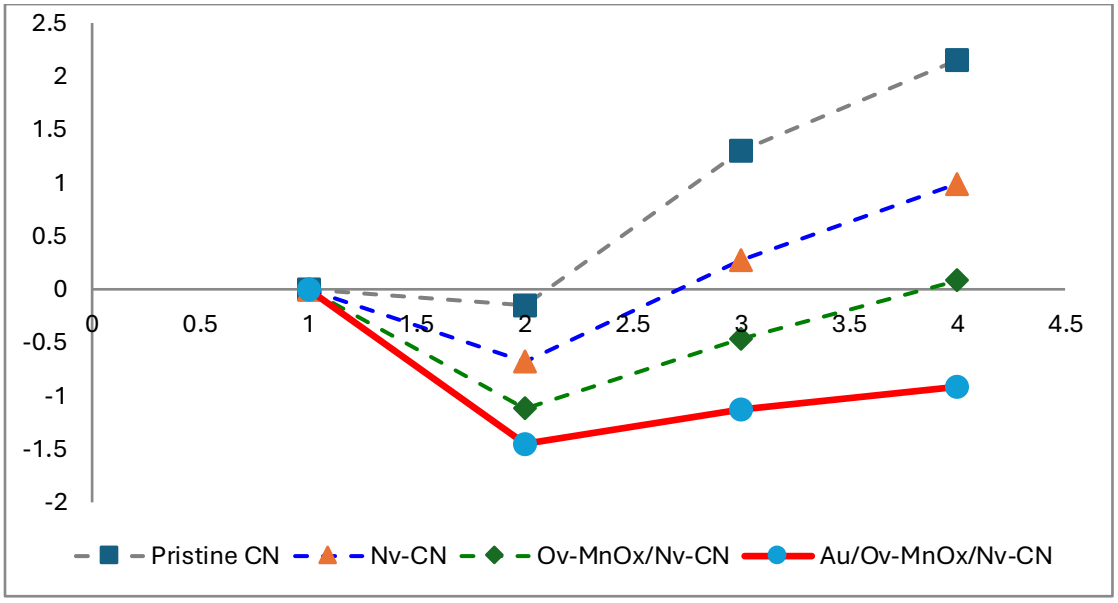

Figure 7: Thermodynamic Energy Profile for CO_2 Reduction Pathway.

Figure 7 show Thermodynamic Energy Profile of CO2 Reduction Pathway Where reaction coordinate diagram is used to visually represent the thermodynamic activation barriers of the sequential steps in CO2 reduction, the results of Table 5. The x-axis follows the progression of the reaction starting with the initial state, adsorption of CO 2, the formation of the radicals of the reaction *COOH (rate-determining step), and the desorption of the final product, *CO. The y-axis is the energy as proportional to free energy in electron volts (eV). The gray line shows that pristine CN has ineffective adsorption as well as extremely high barriers to the formation of intermediates. The energy states reduce greatly as the sophistication of the architecture rises (to blue and green lines). The graph is dominated by the solid red line, which is the Au/Ov-MnOx/Nv-CN catalyst. It immerses itself into negative energy (-1.45 eV) in the adsorption phase, which means aggressive chemisorption of oxygen vacancies. Moreover, the heights of the peaks that depict the *COOH formation and desorption barriers of the *CO are physically flattened (lowered to +0.32 eV and +0.21 eV, respectively). Such value is the final theoretical demonstration that the synergistic plasmon-enhanced photothermal dynamics is the process that is redefining the thermodynamic environment, allowing the reduction reaction itself to become spontaneously feasible.

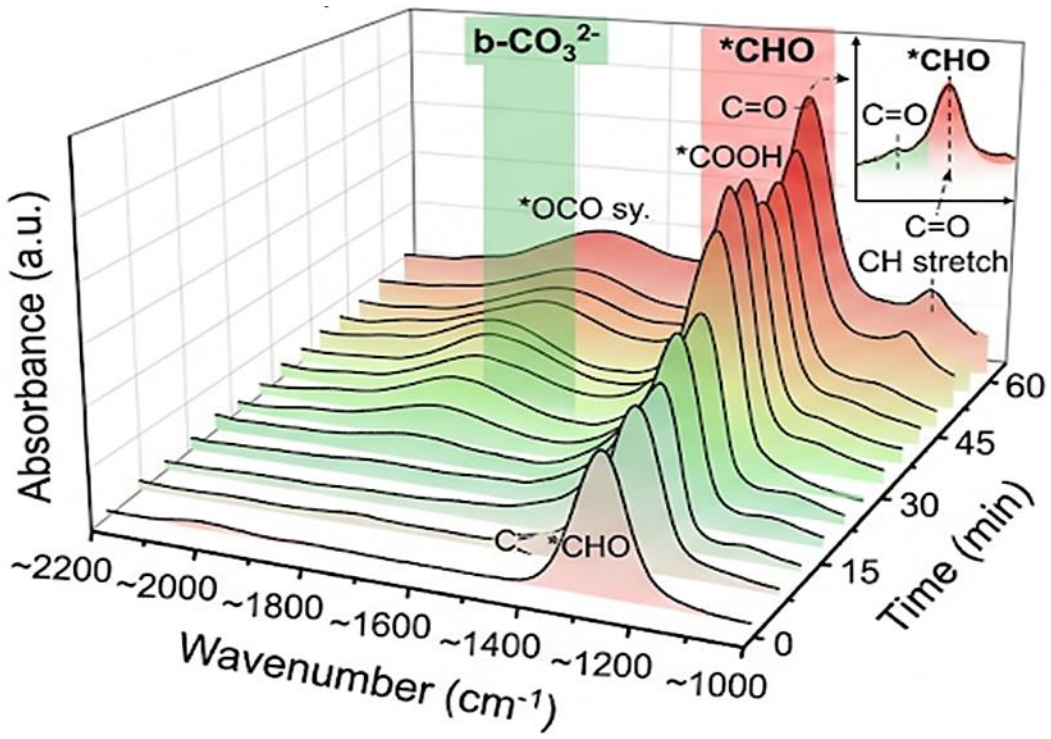

Figure 8: Operando mechanistic investigation of CO2 photoreduction. Time-resolved in-situ DRIFTS spectra recorded over the Au/Ov-MnOx/Nv-CN ternary composite during 60 minutes of continuous light irradiation.

It is a 3D surface plot, which is a visual representation of the dynamic and real-time changes in surface-adsorbed intermediate species during the gas-solid CO2 photoreduction reaction. The absorption irradiation intensities of critical intermediate radicals continue to increase as the irradiation duration advances, within the 60 minute period. Namely, the development of the prominent appearance of the *COOH radical (~1650 cm-1), bidentate carbonate (b-CO3 2 -, ~1430 cm^{-1}), and the appearance of the *CHO intermediate (~1210 cm^{-1}) were monitored by plot. The sequential assembly and concentration of these particular species has offered direct, operando spectroscopic data of the proton-coupled electron transfer (PCET) pathway. This is a clear confirmation of the theoretical multi-electron reduction mechanism and this confirms the fact that the synergistic ternary heterostructure is effectively catalyzing the deep reduction of CO2 to CO and CH4.

5. Discussion

The impressive photocatalytic functionality of the prepared Au/Ov-MnOx/Nv-CN heterostructure yields deep insights in their critical comparison with the current developments in the field of semiconductor-based energy conversion. One of the key pillars of the structural design at the present is the synergistic application of dual-defect engineering. The effectiveness of single-defect systems has been extensively reported in previous studies; an example of how to localize the density of electrons in polymeric carbon nitride is the creation of nitrogen vacancies, which facilitates CO2

photoreduction by activating carbon-oxygen double bonds [21]. Likewise, vacancies at the oxide faces of the transition metal oxides or bismuth-based materials have been used to promote the interfacial charge transfer and atomically monolithic active sites [1, 17]. Nevertheless, the present work has shown that strategic coupling of both Nv and Ov on an interfacial boundary results in a cascaded trapping process, which is significantly more effective than isolated defect systems. In contrast to the structural regulation, which is built only by non-metal co-doping (e.g., phosphorus and carbon) [22] or surface bromination [20], the dual-vacancy design obtained here directly controls the localized work functions of the interacting phases, obliging a spontaneous, unidirectional electron flow, which ideally should obey S-scheme principles.

The dynamics of charge transfer of the Au/Ov-MnOx/Nv-CN composite are an important evolutionary advancement of the traditional heterojunction models. Although direct Z-scheme photocatalysts have been extensively used to preserve strong redox potentials in both environmental and energy aspects [10, 19], recent paradigm shifts heavily favor S- scheme configuration in gas-solid interacial reactions [28]. These sluggish, less energetic charge carriers are selectively removed by the integrated S-scheme physics as confirmed using the Kelvin Probe Force Microscopy and Time-Resolved Photoluminescense data in this study. This is reminiscent of the thermodynamic benefits of the recent S-scheme homojunctions using C-ring infiltrations [24] and ternary heterojunctions to use as photoelectrochemical antibiosis [35]. However, the current design goes beyond these designs by incorporating LSPR-induced hot injection of electrons directly into the highly reductive CO2 reduction conduction band of the defect-rich carbon nitride, retaining an unprecedented driving force.

In addition, light harvesting and local thermal gradient management in the present study differentiates it with traditional photothermal systems. Localized heat generation to help with catalytic conversions has been achieved with carbon dots-infused nanoreactors [8] and synthetic donoracceptor systems [3]. The photothermal processes activated by the Au nanoparticles in the current study are, however, essentially different since the extreme electromagnetic polarization is caused at the broken interface [9]. This plasmonic amplification is useful in closing the gap between the use of visible light and near infrared (NIR) use. Although unlocking the NIR-driven overall water splitting and CO2 reduction is notoriously hard, whether by using dual-LSPR composites [12], multi-level mirror-enhanced nanoapertures to minimize macroscopic heat [14], or parity-forbidden d-d transitions [31], NIR responsiveness can be achieved in the Au/Ov-MnOx/Nv-CN system. Both the macroscopic steady-state temperature of 55.6° C under the sole NIR light conditions attests to the success of the low-energy portion of the solar spectrum in becoming useful to overcome the kinetic activation barriers of the intermediate desorption, an established bottleneck to fundamental plasmonic photocatalysis [11, 15, 23].

The synthesis of CH4 (eight electrons reduction reaction) connotes the unique thermodynamic properties of the designed catalyst mechanistically. It has been found in literature that deep reduction states can be produced with atomically dispersed noble metals [26] or by individual-atom transition metal sites, e.g. copper, being loaded onto polymeric matrices [34]. On the contrary, the present study provides great CH4 selectivity by reducing the formation energy barrier of the *COOH and the desorption barrier of the *CO in a synergistic manner. This is promoted by the deep focusing of the local electron density in the oxygen vacancies, which is disturbed by the strong molecular dipole of crystalline network [2, 7, 33]. The isotopic effects of kinetics and protonation identified in the studies of the advanced CO2 photoreduction are in favor of the fact that the specific type of dense, localised electron cloud offered by the Au LSPR at the Ov-MnOx interface is precisely necessary to overcome the breaking of the carbon-oxygen bond in the initial stage [30].

Lastly, the proposed system presents the photo-corrosion issues that are common in highly active catalysts directly through the operando stability of the system. The regenerative character of the oxygen vacancies accounts for the 96.8% catalytic activity retention that is observed with time of 100 hours. Similarly to the ultrastable reduction driven by visible light with regenerative vacancies in bismuth-based nanosheets [32], the manganese oxide scaffold in the present ternary system can constantly repair its structure through the dynamic exchange of oxygen intermediates throughout the reaction cycle. With the chemically fortified, edge-grafted or highly crystalline form of the carbon nitride [25, 27], the total heterostructure is a virtual destruction-free platform under typical conditions in the process of photocatalysis, avoiding the quick deterioration that is normally seen in the conventional silver-decorated or undecorated crystalline carbon nitride structure [5, 16].

6. Conclusions

The overall growth and careful characterization of the defect-modulated Manganese Oxide/Carbon Nitrate heterostructure, optimally combined with plasmonic Gold nanoparticles, is a radical step in the direction of solar-driven chemical synthesis. This study has been able to establish that it is the specific atomic engineering of dual intrinsic defects that form an exceptionally strong internal electric field that are namely nitrogen vacancies in highly crystalline carbon nitride framework and regenerative oxygen vacancies in ultrathin manganese oxide nanosheets. This tailored electronic environment smoothly leads to a Step-scheme charge transfer process, in essence eliminating the ubiquitous problem of rapid electron-hole recombination, and fully conserving the highly energetic charge carriers which is needed to drive deep reduction of the molecules. Localized surface plasmon resonance created by the introduction of Gold nanoparticles radically changes the thermodynamics of the gas-solid interface. The high electromagnetic polarization, combined with the dramatic localized photothermal heating, is an aggressive Kinetic amplifier. This multiple plasmonic-photothermal effect does not only periodically broaden the spectrum of light-harvesting

as far into the near-infrared as possible; but also provides the essential thermal kinetic energy necessary to overcome the drastic activation barriers to the creation of intermediate radicals and the desorption of carbon monoxide. As a result, the ternary system designed has unprecedented evolution rates of carbon monoxide and methane, which is a great improvement compared to traditional binary heterojunctions and isolated defect systems. The regenerative, continuous nature of the oxygen vacancies has made sure that the catalyst is structurally clean and operationally robust throughout long continuous operation periods, and in fact, it is completely resistant to photo-corrosion as occurs in traditional systems. This work ultimately offers an extremely conclusive, thermodynamically confirmed architectural design of exploiting the synergistic interaction of atomic defect control, superior charge transfer physics, non-radiative plasmonic relaxation, next-generation high-efficiency technology of valorizing carbon dioxide in the atmosphere.

References:

[1] Li, C., Zhang, P., Gu, F., Tong, L., Jiang, J., Zuo, Y., & Dong, H. (2023). Atomically dispersed Au confined by oxygen vacancies in Au-θ-Al2O3/Au/PCN hybrid for boosting photocatalytic CO2 reduction driven by multiple built-in electric fields. *Chemical Engineering Journal*, *476*, 146514. https://doi.org/10.1016/j.cej.2023.146514

[2] Li, G., Wu, Y., Wang, M., Zhou, W., Liu, X., Zhu, Z., ... & Huo, P. (2023). Graphitic carbon nitride modified with 2-aminothiophene-3-carbonitrile to boost molecular dipole and n→ π* electronic transition for photoreduction of carbon dioxide. *ACS Applied Nano Materials*, *6*(15), 14513-14526. https://doi.org/10.1021/acsanm.3c02600

[3] Song, X., Li, G., Zhou, W., Wu, Y., Liu, X., Zhu, Z., ... & Wang, M. (2024). Construction of Au-modified CN-based donor-acceptor system coupled with dual photothermal effects for efficient photoreduction of carbon dioxide. *Journal of Colloid and Interface Science*, *664*, 868-881. https://doi.org/10.1016/j.jcis.2024.03.090

[4] Wu, H., Liang, R., Song, G., Hu, Z., Zhang, X., & Zhou, M. (2024). Enhanced interfacial charge transfer on Bi metal@ defective Bi2Sn2O7 quantum dots towards improved full-spectrum photocatalysis: A combined experimental and theoretical investigation. *Chinese Chemical Letters*, *35*(6), 109131. https://doi.org/10.1016/j.cclet.2023.109131

[5] Gao, S.; Liu, S.; Wang, D.; Zhu, C.; Shi, W.; Tao, H.; Wang, X.; Yang, F. Boosting carrier separation over ultrathin g-C3N4 by f-ionic intercalation for improved photocatalytic activity. Appl. Surf. Sci. 2024, 644, 158808. https://doi.org/10.1016/j.apsusc.2023.158808

[6] Tang, X., Shen, W., Li, D., Li, B., Wang, Y., Song, X., ... & Huo, P. (2023). Research on cobalt-doping sites in g-C3N4 framework and photocatalytic reduction CO2 mechanism insights. *Journal of Alloys and Compounds*, *954*, 170044. https://doi.org/10.1016/j.jallcom.2023.170044

[7] Zeng, W., Dong, Y., Ye, X., Zhang, Z., Zhang, T., Guan, X., & Guo, L. (2024). Crystalline carbon nitride with in-plane built-in electric field accelerates carrier separation for excellent photocatalytic hydrogen evolution. *Chinese Chemical Letters*, *35*(4), 109252. https://doi.org/10.1016/j.cclet.2023.109252

[8] Sun, X., Chen, Z., Shen, Y., Qin, H., Yuan, H., Lu, J., ... & Shi, W. (2024). Efficient photothermal-assisted photocatalytic H2 production using carbon dots-infused g-C3N4 nanoreactors synthesized via one-step template-free thermal polymerization. *Chemical Engineering Journal*, *488*, 151041. https://doi.org/10.1016/j.cej.2024.151041

[9] Gao, Y., Nie, W., Zhu, Q., Wang, X., Wang, S., Fan, F., & Li, C. (2020). The polarization effect in surface-plasmon-induced photocatalysis on Au/TiO2 nanoparticles. *Angewandte Chemie*, *132*(41), 18375-18380. https://doi.org/10.1002/ange.202007706

[10] Li, X., Jiang, H., Ma, C., Zhu, Z., Song, X., Wang, H., ... & Li, X. (2021). Local surface plasma resonance effect enhanced Z-scheme ZnO/Au/g-C3N4 film photocatalyst for reduction of CO2 to CO. *Applied Catalysis B: Environmental*, *283*, 119638. https://doi.org/10.1016/j.apcatb.2020.119638

[11] Vu, N. N., Kaliaguine, S., & Do, T. O. (2020). Plasmonic photocatalysts for sunlight-driven reduction of CO2: Details, developments, and perspectives. *ChemSusChem*, *13*(16), 3967-3991. https://doi.org/10.1002/cssc.202000905 https://doi.org/10.1002/cssc.202000905

[12] Zhao, L., Liu, Y., Xi, X., Nie, Z., yee Lim, F., Ong, S. L., & Hu, J. (2024). Design of dual-LSPR Bi/W18O49 composite and its red-light driven photocatalytic property in the photocatalytic degradation of PPCPs. *Chemical Engineering Journal*, *481*, 148119. https://doi.org/10.1016/j.cej.2023.148119

[13] Huang, Y., Yang, H., Lu, X., Chen, M., & Shi, W. (2024). Near infrared-driven photocatalytic overall water splitting: Progress and perspective. *Chinese Journal of Catalysis*, *58*, 105-122. https://doi.org/10.1016/S1872-2067(23)64594-2

[14] Anyika, T., Hong, I., & Ndukaife, J. C. (2023). Mirror-enhanced plasmonic nanoaperture for ultrahigh optical force generation with minimal heat generation. *Nano letters*, *23*(24), 11416-11423. https://doi.org/10.1021/acs.nanolett.3c02543

[15] Kumar, A., Choudhary, P., Kumar, A., Camargo, P. H., & Krishnan, V. (2022). Recent advances in plasmonic photocatalysis based on TiO2 and noble metal

nanoparticles for energy conversion, environmental remediation, and organic synthesis. *Small*, *18*(1), 2101638. https://doi.org/10.1002/smll.202101638

[16] Pan, Z., Ding, W., Chen, H., & Ji, H. (2024). A review on g-C3N4 decorated with silver for photocatalytic energy conversion. *Chinese Chemical Letters*, *35*(2), 108567. https://doi.org/10.1016/j.cclet.2023.108567

[17] Wang, F., Guo, J., Han, L., Shen, H., Zhu, L., & Chen, S. (2023). Oxygen vacancy-engineered BiOCl nanoflake with silver decoration for enhanced photocatalytic CO2 reduction at solid-gas interface. *Chemical Engineering Journal*, *478*, 147365. https://doi.org/10.1016/j.cej.2023.147365

[18] Li, S., Wang, Y., Wang, J., Kirk, C. H., Wang, H., Sun, J., ... & Li, B. (2023). Efficient photocatalytic hydrogen evolution reaction promoted via a synergistic strategy of S-scheme heterojunction structure combined with surface plasmon resonance effect. *Chemical Engineering Journal*, *466*, 143184. https://doi.org/10.1016/j.cej.2023.143184

[19] Fu, X.; Huang, H.; Tang, G.; Zhang, J.; Sheng, J.; Tang, H. Recent advances in g-C3N4-based direct Z-scheme photocatalysts for environmental and energy applications. Chin. J. Struct. Chem. 2024, 43, 100214. https://doi.org/10.1016/j.cjsc.2024.100214

[20] Yan, P., Ji, F., Zhang, W., Mo, Z., Qian, J., Zhu, L., & Xu, L. (2023). Engineering surface bromination in carbon nitride for efficient CO2 photoconversion to CH4. *Journal of Colloid and Interface Science*, *634*, 1005-1013. https://doi.org/10.1016/j.jcis.2022.12.063

[21] Yang, Z., Zhang, Y., Zhang, H., Zhao, J., Shi, H., Zhang, M., ... & Yang, P. (2022). Nitrogen vacancies in polymeric carbon nitrides promote CO2 photoreduction. *Journal of Catalysis*, *409*, 12-23. https://doi.org/10.1016/j.jcat.2022.03.016

[22] Huang, Q. S., Li, Q., Chu, C., Liu, Q., Li, Z., & Mao, S. (2024). Synergetic regulation of electronic structure of graphitic carbon nitride through phosphorus and carbon co-doping for enhanced photocatalytic CO2 reduction. *Chemical Engineering Journal*, *482*, 149155. https://doi.org/10.1016/j.cej.2024.149155

[23] Li, J., Lou, Z., & Li, B. (2022). Nanostructured materials with localized surface plasmon resonance for photocatalysis. *Chinese Chemical Letters*, *33*(3), 1154-1168. https://doi.org/10.1016/j.cclet.2021.07.059

[24] Yu, Z., Guan, C., Yue, X., & Xiang, Q. (2023). Infiltration of C-ring into crystalline carbon nitride S-scheme homojunction for photocatalytic hydrogen evolution. *Chinese Journal of Catalysis*, *50*, 361-371. https://doi.org/10.1016/S1872-2067(23)64448-1

[25] Gu, Y., Feng, H., Zhao, J., Cui, M., Li, Y., & Li, Z. (2023). Rational construction of edge-grafted g-C3N4 via cross-linking aromatic compounds with CF bonds for

efficient photocatalytic H2 evolution. *Chemical Engineering Journal*, *476*, 146555. https://doi.org/10.1016/j.cej.2023.146555

[26] Lei, J., Zhou, N., Sang, S., Meng, S., Low, J., & Li, Y. (2024). Unraveling the roles of atomically-dispersed Au in boosting photocatalytic CO2 reduction and aryl alcohol oxidation. *Chinese Journal of Catalysis*, *65*, 163-173. https://doi.org/10.1016/S1872-2067(24)60109-9

[27] Zhang, Y., Wu, L., Wang, S., Yang, D., Liang, H., Wu, Y., ... & Wang, Y. (2024). Enhanced visible-light photocatalytic hydrogen evolution using two-dimensional carbon nitride sheets with the removal of amine groups. *Chinese Chemical Letters*, *35*(2), 108551. https://doi.org/10.1016/j.cclet.2023.108551

[28] Niu, Q., Dong, S., Tian, J., Huang, G., Bi, J., & Wu, L. (2022). Rational design of novel COF/MOF S-scheme heterojunction photocatalyst for boosting CO2 reduction at gas–solid interface. *ACS Applied Materials & Interfaces*, *14*(21), 24299-24308. https://doi.org/10.1021/acsami.2c02439

[29] Zhang, J., Li, Y., Zhao, X., Wang, L., Chen, H., Wang, S., ... & Sun, H. (2021). Aligning potential differences within carbon nitride based photocatalysis for efficient solar energy harvesting. *Nano Energy*, *89*, 106357. https://doi.org/10.1016/j.nanoen.2021.106357

[30] Yin, S., Zhou, Y., Liu, Z., Wang, H., Zhao, X., Zhu, Z., ... & Huo, P. (2024). Elucidating protonation pathways in CO2 photoreduction using the kinetic isotope effect. *Nature Communications*, *15*(1), 437. https://doi.org/10.1038/s41467-024-44753-x

[31] Li, X., Li, L., Chen, G., Chu, X., Liu, X., Naisa, C., ... & Feng, X. (2023). Accessing parity-forbidden d-d transitions for photocatalytic CO2 reduction driven by infrared light. *Nature Communications*, *14*(1), 4034. https://doi.org/10.1038/s41467-023-39666-0

[32] Zu, X., Zhao, Y., Li, X., Chen, R., Shao, W., Wang, Z., ... & Xie, Y. (2021). Ultrastable and efficient visible-light-driven CO2 reduction triggered by regenerative oxygen-vacancies in Bi2O2CO3 nanosheets. *Angewandte Chemie International Edition*, *60*(25), 13840-13846. https://doi.org/10.1002/anie.202101894

[33] Liu, J., Fu, W., Liao, Y., Fan, J., & Xiang, Q. (2021). Recent advances in crystalline carbon nitride for photocatalysis. *Journal of Materials Science & Technology*, *91*, 224-240. https://doi.org/10.1016/j.jmst.2021.03.017

[34] Wang, Z., Zhang, M., Hu, J., Li, Z., Zhang, W., Zhang, J., ... & Lu, Z. (2023). Polymeric carbon nitride loaded with atomic Cu sites for improved CO2 photocatalytic conversion performance. *Journal of Power Sources*, *577*, 233188. https://doi.org/10.1016/j.jpowsour.2023.233188

[35] Ren, X., Guo, M., Xue, L., Xu, L., Li, L., Yang, L., ... & Wang, Y. (2023). Photoelectrochemical performance and S-scheme mechanism of ternary GO/g-C3N4/TiO2 heterojunction photocatalyst for photocatalytic antibiosis and dye degradation under visible light. *Applied Surface Science*, *630*, 157446. https://doi.org/10.1016/j.apsusc.2023.157446